

1 **The evolving outer heliosphere: Large-scale stability and time**
2 **variations observed by the Interstellar Boundary Explorer**

3 D.J. McComas^{1,2}, M. Bzowski³, P. Frisch⁴, G.B. Crew⁵, M.A. Dayeh¹, R. DeMajistre⁶,
4 H.O. Funsten⁷, S.A. Fuselier⁸, M. Gruntman⁹, P. Janzen¹⁰, M.A. Kubiak³, G. Livadiotis¹,
5 E. Möbius¹¹, D.B. Reisenfeld¹⁰, N.A. Schwadron^{12,1}

6

7 ¹ *Southwest Research Institute, P.O. Drawer 28510, San Antonio, TX 78228, USA*

8 (dmccomas@swri.org)

9 ² *University of Texas at San Antonio, San Antonio, TX 78249, USA*

10 ³ *Space Research Centre of the Polish Academy of Sciences, Bartycka 18A, 00-716,*

11 *Warsaw, Poland*

12 ⁴ *University of Chicago, Department of Astronomy and Astrophysics, 5640 S. Ellis Ave.,*

13 *Chicago, IL 60637, USA*

14 ⁵ *Massachusetts Institute of Technology, Kavli Institute for Astrophysics and Space*

15 *Research, 77 Massachusetts Avenue, 37-515, Cambridge, MA, 02139, USA*

16 ⁶ *Applied Physics Laboratory, Johns Hopkins University, 11100 Johns Hopkins Road,*

17 *Laurel, MD 20723, USA*

18 ⁷ *Los Alamos National Laboratory, Los Alamos, Bikini Atoll Rd., SM 30, NM 87545, USA*

19 ⁸ *Lockheed Martin Advanced Technology Center, 3251 Hanover St, Palo Alto, CA 94304,*

20 *USA*

21 ⁹ *University of Southern California, Division of Astronautical Engineering, Viterbi*

22 *School of Engineering, RRB 224, 1192, Los Angeles, CA 90089, USA*

23 ¹⁰ *University of Montana, 32 Campus Drive, Missoula, MT, USA*

24 ¹¹ *University of New Hampshire, Space Science Center, Morse Hall Rm 407, Durham,*
25 *NH 03824, USA*

26 ¹² *Boston University, 725 Commonwealth Avenue, CAS Bulding, Room 515, Boston, Mass,*
27 *02215 USA*

28

29 Abstract. The first all-sky maps of Energetic Neutral Atoms (ENAs) from the Interstellar
30 Boundary Explorer (IBEX) exhibited smoothly varying, globally distributed flux and a
31 narrow “ribbon” of enhanced ENA emissions. In this study we compare the second set of
32 sky maps to the first in order to assess the possibility of temporal changes over the six
33 months between views of each portion of the sky. While the large-scale structure is
34 generally stable between the two sets of maps, there are some remarkable changes that
35 show that the heliosphere is also evolving over this short timescale. In particular, we find
36 that 1) the overall ENA emissions coming from the outer heliosphere appear to be
37 slightly lower in the second set of maps compared to the first, 2) both the north and south
38 poles have significantly lower (~10-15%) ENA emissions in the second set of maps
39 compared to the first across the energy range from 0.5-6 keV, and 3) the “knot” in the
40 northern portion of the ribbon in the first maps is less bright and appears to have spread
41 and/or dissipated by the time the second set was acquired. Finally, the spatial distribution
42 of fluxes in the southern-most portion of the ribbon has evolved slightly, perhaps moving
43 as much as 6° (one map pixel) equatorward on average. The observed large-scale stability
44 and these systematic changes at smaller spatial scales provide important new information
45 about the outer heliosphere and its global interaction with the galaxy and help inform
46 possible mechanisms for producing the IBEX ribbon.

47 **1. Introduction**

48 The Interstellar Boundary Explorer (IBEX) mission (see *McComas et al.* [2009a] and
49 other papers in the IBEX Special Issue of Space Science Reviews) recently provided the
50 first global observations of the heliosphere's interstellar interaction. These observations
51 included energy-resolved, all-sky images of energetic neutral atoms (ENAs) over the
52 energy range from ~ 0.1 -6 keV, emanating from the outer heliosphere [*McComas et al.*,
53 2009b; *Fuselier et al.*, 2009; *Funsten et al.*, 2009a; *Schwadron et al.*, 2009]. Generally
54 speaking, while some aspects of IBEX ENA observations were consistent with prior
55 expectations, many were not. In particular, IBEX discovered a narrow "ribbon" of
56 significantly enhanced ENA emissions passing between the directions of the two
57 Voyager spacecraft in the sky. Additional observations at higher energies from the
58 Cassini spacecraft [*Krimigis et al.*, 2009] indicate a broader band of enhanced emissions
59 that generally lies close to the IBEX ribbon near the equator and in the northern
60 hemisphere, but deviates significantly from the ribbon in the south. Finally, the first
61 direct measurements of interstellar neutral H and O were also made by IBEX [*Möbius et*
62 *al.*, 2009]. In this study, we provide new ENA observations from IBEX, covering its
63 complete second set of sky maps, and focus on determining if and how these maps (and
64 the outer heliosphere itself) may be evolving over short (half-year) timescales.

65

66 The narrow ribbon discovered by IBEX is superposed on a globally distributed ENA flux
67 that is organized by ecliptic latitude and longitude (essentially solar latitude and the
68 direction of motion with respect to the local interstellar medium, LISM) [*McComas et al.*,
69 2009b; *Fuselier et al.*, 2009; *Funsten et al.*, 2009a; *Schwadron et al.*, 2009]. ENA fluxes

70 in the ribbon reach maxima ~2-3 times higher than the surrounding regions, and while the
71 ribbon is variable in width from $<15^\circ$ to $>25^\circ$ FWHM along its length [McComas et al.,
72 2009b; Fuselier et al., 2009], it averages $\sim 20^\circ$ wide over a broad energy range of IBEX's
73 energy steps centered on energies from 0.7-2.7 keV [Fuselier et al., 2009]; this analysis
74 did not remove the intrinsic width of the IBEX sensors' angular response ($\sim 7^\circ$ FWHM),
75 so the real average width of the ribbon is actually thinner $<20^\circ$. Even more remarkably,
76 the ribbon also shows statistically significant fine structure that is at most a few degrees
77 across [McComas et al., 2009b]. The center of the ribbon passes $\sim 25^\circ$ away from the
78 upwind direction or "nose" of the heliosphere and has brighter emissions from somewhat
79 broader regions at higher latitudes in both hemispheres - around $\sim 60^\circ$ N and $\sim 40^\circ$ S
80 ecliptic latitudes [McComas et al., 2009b; Funsten et al., 2009a]. The northern bright
81 region or "knot" has a different spectral shape than the rest of the ribbon with an
82 enhancement (bump) at higher energies, consistent with the shape of other near-pole
83 energy spectra [Funsten et al., 2009a]. In fact, the ribbon has nearly the same average
84 spectral slope and shape as surrounding regions at all heliolatitudes [McComas et al.,
85 2009b; Funsten et al., 2009a].

86

87 One of IBEX's remarkable discoveries about the ribbon is that it appears to be ordered by
88 the most likely direction of the interstellar magnetic field just outside the heliopause (\mathbf{B}),
89 and in particular seems to lie where \mathbf{B} is nearly perpendicular to IBEX's radially directed
90 (\mathbf{r}) line of sight (LOS) – that is where $\mathbf{B} \cdot \mathbf{r} = 0$ [McComas et al., 2009b; Schwadron et al.,
91 2009]. This direction is based on inferred flow deflections between interstellar H and He
92 [Lallement et al., 2005], which are also consistent with the direction inferred from 2-3

93 kHz radio emissions measured by the Voyager spacecraft [Gurnett et al., 2006]. The
94 model of the draped, local magnetic field [Pogorelov et al., 2009] that very closely
95 matches the IBEX ribbon [Schwadron et al., 2009] incorporates these flow deflections,
96 the observed ~ 10 AU difference between the termination shock (TS) crossing distances
97 of Voyagers 1 and 2 [Stone et al., 2008], and the inferred interstellar densities just outside
98 the heliosphere [Slavin and Frisch, 2008; Bzowski et al., 2008].

99

100 The ribbon weakens, but continues to extend around the north ecliptic pole, nearly
101 closing a loop on the sky [McComas et al., 2009b; Funsten et al., 2009a; Schwadron et
102 al., 2009]. The “center” of this loop in the first set of IBEX sky maps is at $\sim 39^\circ$ ecliptic
103 latitude and $\sim 221^\circ$ ecliptic longitude [Funsten et al., 2009a]. Ultimately, the combination
104 of simulations of detailed draping and compression of the interstellar field [e.g.,
105 Pogorelov et al., 2009; Schwadron et al., 2009 and references therein] with multiple sets
106 of all-sky maps from IBEX will likely provide the most accurate direction of the local
107 interstellar magnetic field.

108

109 The IBEX observations show the brightest regions of ribbon at mid to high latitudes,
110 where slow and fast solar winds interact in corotating interaction regions (CIRs). Thus, it
111 seems likely that the ribbon emissions are at least partially related to the solar wind
112 properties as well as to the external environment. Finally, as pointed out by McComas et
113 al. [2009b], while the ribbon appears as a generally continuous region of emissions, it
114 could easily be a string of localized and sometimes overlapping “knots” of emission. In

115 fact, the fine structure in the ribbon suggests that whatever mechanism creates the ribbon
116 emissions must be highly spatially variable.

117

118 Various possible explanations for the source of the ribbon were identified by *McComas et*
119 *al.* [2009], with additional analysis on several of these provided by *Fuselier et al.* [2009],
120 *Funsten et al.* [2009a], and *Schwadron et al.* [2009]. These explanations spanned
121 possibilities of how the ribbon emissions might be generated in the inner heliosheath
122 (between the TS and heliopause) in the solar wind (inside the TS), and in the outer
123 heliosheath (beyond the heliopause). The six possible sources of the IBEX ribbon
124 identified and briefly discussed by *McComas et al.* [2009b] are summarized
125 schematically in Figure 1 and described below:

126

127 (1) Maximum Pressure and Stagnation

128 The first general area of possible explanations centers on the observations of enhanced
129 particle pressure within the ribbon [*McComas et al.*, 2009; *Funsten et al.*, 2009a;
130 *Schwadron et al.*, 2009]. This enhanced pressure could be generally balanced by
131 enhanced external pressure from the combination of the external plasma dynamic and
132 magnetic ($J \times B$) forces, producing a localized band of maximum total pressure around the
133 heliopause. Such enhanced pressure at the heliopause might propagate throughout the
134 inner heliosheath, adjusting the plasma properties and bulk flow in such a way that the
135 ribbon might indicate the true region of highest pressure in the inner heliosheath. If so,
136 the flow would stagnate in this region and ion densities and ENA emissions would be
137 enhanced. As pointed out by *McComas et al.* [2009b], if the ribbon does represent the

138 region of highest pressure, then it would divide flows through the inner heliosheath,
139 analogous to a continental divide, which might explain the unusual flow directions
140 observed at the locations of the two Voyager spacecraft in the inner heliosheath.
141
142 An extension of this concept discussed by these authors was that the additional pressure
143 might also extrude small regions of the heliopause forming limited outward bulges in the
144 heliopause in the regions where the field was laying most tightly along its surface; such
145 “herniations” might collect ions, producing very high densities and almost no bulk flow,
146 potentially explaining the observed fine structure. This general explanation could
147 naturally account for the fact that the ribbon has a very similar spectral slope and shape of
148 the surrounding regions, as the enhanced ENA flux would arise naturally from the
149 accumulation of particles already in the inner heliosheath. Simulations and observations
150 appear to be at odds with one another concerning this mechanism. On the other hand,
151 magnetohydrodynamic (MHD) simulations of the heliospheric interaction, including
152 kappa distributions to emulate effects of enhanced tails of higher-energy pickup ions
153 [*Prested et al.*, 2008; *Izmodenov et al.*, 2009; *Pogorelov et al.*, 2009], indicate maximum
154 pressure in the inner heliosheath near the nose and not along an extended region
155 significantly offset from the nose, such as the ribbon. Surely, the actual conditions in the
156 inner heliosheath are more complicated than accounted for in the current models, with (as
157 initially suggested by *Zank et al.* [1996]) a much smaller (~20% by number) pickup ion
158 population receiving the vast majority of the energization at the TS [*Richardson et al.*,
159 2008; 2009]. A start was made at more carefully addressing the role of the TS in
160 processing the solar wind and PUIs [*Zank et al.*, 2010], however much more theoretical

161 work is needed in this area. Perhaps the complete treatment of this far more complicated
162 plasma in future simulations will reduce the discrepancies between the simulations and
163 observations.

164

165 (2) Primary ENAs from Compression

166 Another pair of related explanations [(2) and (3)] invoke the possibility of ribbon
167 emissions coming from outside the heliopause, from regions where the external $\mathbf{B} \cdot \mathbf{r} = 0$
168 [McComas et al., 2009b; Schwadron et al., 2009] (see above). Compression of the
169 external field would increase densities and provide perpendicular heating, producing
170 more perpendicular pitch-angle distributions (enhanced particles around 90° pitch angles)
171 where they would preferentially emit in a plane that includes the inward radial direction.
172 Thus, local compressions in the outer heliosheath magnetic field would preferentially
173 emit ENAs that would be observable in the inner heliosphere by IBEX in exactly the
174 regions where the average external field is most perpendicular to the radial LOS.

175

176 (3) Secondary ENAs

177 In addition to interstellar ions, the external magnetic field is populated with particles from
178 ionization of outward traveling ENAs from both the solar wind region inside the TS and
179 the inner heliosheath. This source is labeled “secondary ENAs” as they have been
180 through the ion-to-ENA conversion process twice. These ions would have relatively
181 perpendicular pitch-angle distributions and be further compressed in regions where $\mathbf{B} \cdot \mathbf{r} =$
182 0. The primary problem with this process for producing the ribbon, as pointed out by
183 McComas et al. [2009b], is that pitch-angle distributions would need to remain nearly

184 perpendicular for times comparable to or longer than neutralization times in the outer
185 heliosheath – times typically thought to be a few years. A simulation by *Izmodenov et al.*
186 [2009] including the secondary ENA source assumed comparatively rapid isotropization
187 and did not produce a ribbon-like structure. Since the publication of the IBEX results,
188 however, two different 3D MHD simulations [*Heerikhuisen et al.*, 2010; *Chalov et al.*,
189 2010] have produced a structure very much like the overall ribbon structure by assuming
190 that perpendicular pitch-angle distributions can survive long enough for ions to re-
191 neutralize. If this assumption could somehow be validated, this secondary ENA process
192 would be a highly viable explanation for producing the ribbon. Finally, generating
193 observed fine structure in the ribbon with this process would further require bunched
194 ENAs produced by initially bunched solar wind ions or pickup ions, or additional small-
195 scale compressions of the magnetic field as discussed in (2).

196

197 (4) ENAs from Magnetic Reconnection at the Heliopause

198 Another possible mechanism identified by *McComas et al.* [2009b] was that ribbon
199 ENAs might result from magnetic reconnection across the heliopause. Reconnection
200 would allow hot heliosheath ions to propagate out into cooler, denser outer heliosheath
201 plasma. Magnetic reconnection could produce narrowly confined magnetic structures
202 potentially consistent with both “knots” and fine structure observed in the ribbon. The
203 external pressure is greatest along the ribbon [*Schwadron et al.*, 2009], which generally
204 enhances the rate of magnetic reconnection. However, the magnetic field in the inner
205 heliosheath is highly variable [*Burlaga et al.*, 2006], and average the field just inside of
206 the heliopause is expected to be “painted” with narrow alternating bands of oppositely

207 directed field [Suess, 2004], so it is not obvious why reconnection would be limited to a
208 narrow structure like the ribbon.

209

210 (5) ENAs from Shock-Accelerated Pickup Ions

211 Yet another possible mechanism discussed by *McComas et al.* [2009b] was that the
212 ribbon ENAs might be coming from the region around the TS, perhaps from shock-
213 accelerated pickup ions [Chalov and Fahr, 1996; Fahr et al., 2009] propagating inward
214 through the region where the solar wind decelerates significantly (~20%) in the last ~10
215 AU just inside the TS [Richardson et al., 2008]. Again, however, it is not obvious why
216 this mechanism would produce a ribbon instead of broadly distributed regions of
217 enhanced emissions.

218

219 6) ENAs from Heliopause Instabilities

220 Finally, *McComas et al.* [2009b] suggested that large-scale, Rayleigh-Taylor and/or
221 Kelvin–Helmholtz-like instabilities might confine hot, inner-heliosheath plasma in
222 narrow structures along the heliopause boundary. Such instabilities can be driven by
223 neutrals destabilizing the boundary. Some models [e.g., Borovikov et al., 2008] produce
224 large (>10 AU), semicoherent structures with higher ion densities that move tailward at
225 tens of km s^{-1} along the heliopause boundary.

226

227 The various possible mechanisms are not mutually exclusive; in fact some combination
228 or combinations may well ultimately explain the ribbon. One such example that is being
229 actively pursued [*Kucharek et al.*, in preparation] combines (1) and (5). If a pressure

230 maximum (1) propagates through the inner heliosheath and indents the TS, ions that
231 specularly reflect off the indented part of the TS (as part of the shock-formation process)
232 will have gyro-velocity vectors directed back towards the Sun (5). ENAs produced by
233 charge exchange of these ions may account for the ribbon and fine structure within it.

234

235 While the basic mechanisms delineated above are under consideration for explaining the
236 IBEX ribbon, none produces the full range of observations without making significant,
237 unsubstantiated assumptions, and perhaps the ribbon arises from some completely
238 different mechanism. In fact, a seventh possible mechanism has been suggested by
239 *Grzedzielski et al.* [2010]. These authors propose a novel interpretation where the ribbon
240 does not arise from the heliospheric interaction at all, but instead from ENAs produced
241 by charge exchange between neutral H atoms at the nearby edge of the local interstellar
242 cloud (LIC) and hot protons from the Local Bubble. They argue that for reasonable
243 assumptions about local densities, such galactic ENAs should be able to reach the
244 heliosphere provided that the edge is close enough (less than ~ 500 - 2000 AU).

245

246 While IBEX data support some earlier ideas, in other areas a completely new paradigm is
247 needed for understanding the interaction between our heliosphere and the galactic
248 environment. This study examines the possibility of time evolution of the heliospheric
249 interaction in general and IBEX ribbon in particular, by comparing the first set of six-
250 month IBEX sky maps with the new set of maps generated over the subsequent six
251 months of observations. Observations of temporal evolution in IBEX ENA measurements

252 are pivotal for understanding this interaction in general and for testing the various
253 hypotheses that may account for the unexpected structures, such as the ribbon.

254

255 **2. Observations from IBEX**

256 IBEX is a spinning spacecraft with a spin rate of 4 RPM and spin axis (and solar array)
257 pointed toward the Sun. Each orbit (orbital period ~ 7.5 days) around perigee, the spin
258 axis is repointed back toward the Sun to compensate for the $\sim 1^\circ/\text{day}$ drift as the Earth
259 orbits the Sun. Therefore, observations from each orbit provide $\sim 7^\circ$ -wide “swaths”, at
260 multiple energies, that collectively produce a set of all-sky maps each six months. The
261 full width half maximum (FWHM) angular resolution of the IBEX ENA cameras is also
262 $\sim 7^\circ$, so, by design, the repointing and intrinsic angular resolution are roughly matched. In
263 this study we show observations from the IBEX-Hi sensor for energy steps (or
264 passbands) 2-6; Table 1 provides the nominal (peak) energy and energy range of each
265 energy step [Funsten et al., 2009b]. Detailed information about all aspects of the mission
266 is available in McComas et al. [2009a] and other papers in the IBEX Special Issue of
267 Space Science Reviews.

268

269 Figure 2 schematically shows the geometry of the IBEX orbit over the year. The Earth’s
270 magnetosphere (shaded) is oriented away from the Sun, so different seasons have quite
271 different magnetospheric backgrounds and obscuration. The first maps were made while
272 IBEX’s apogee was largely on the sunward side of Earth, where much of the time IBEX
273 was outside the Earth’s bow shock and in the solar wind. The second set of sky maps
274 were produced from orbits as IBEX’s apogee crossed through the magnetotail.

275 Commissioning of the IBEX-Hi sensor [Funsten et al., 2009b] was completed in Orbit 10,

276 so the first sky maps were taken over Orbits 11-33 (25 December 2008 through 18 June
277 2009), while the second were from Orbits 34-56 (18 June through 10 December 2009).
278
279 Figure 3 provides a comparison of the first (left) and second (right) sets of sky maps in
280 the spacecraft frame of reference. From top to bottom, the maps show data in the top five
281 energy channels of IBEX-Hi, labeled with the nominal central energies for each passband
282 (See Table 1). For each energy step, maps are compared using a consistent color scale.
283 While some corrections are required to make quantitative comparisons between maps at
284 each energy, the uncorrected observations in Figure 3 clearly show generally similar
285 ENA fluxes and the presence of the ribbon in roughly the same location for both the first
286 and second maps.

287

288 In order to quantitatively compare sky maps taken six months apart, we first consider
289 processes that could affect the measured fluxes of ENAs at IBEX. These include: 1) the
290 finite probability of ionization of ENAs on their way into 1 AU from the outer
291 heliosphere; 2) a very small energy change of ENAs due to the combined actions of solar
292 gravity and radiation pressure; and 3) the finite speed of the proper motion of the IBEX
293 detectors with respect to the Sun (the Compton-Getting effect). The first two of these
294 effects can be significant at lower energies, but only have very minor influence on the
295 ENAs in the energy ranges examined here (~ 0.5 -6 keV). This is particularly true for quiet
296 times of the Sun and the solar wind, in which both the ionization probability and radiation
297 pressure are smallest. The past several years have been amongst the quietest times
298 observed with the most prolonged, lowest power interval of solar wind since the start of
299 the space age [McComas et al., 2008]. While these two effects are at work at all distances

300 along the trajectory of an ENA, they have the largest quantitative impact over the last ~10
301 AU as ENAs travel through the inner heliosphere approaching IBEX.

302

303 For this study, we calculated the combined effects of ionization and gravity/solar wind
304 pressure using recent solar observations from the Timed/SEE series (Lyman-alpha,
305 [Woods et al., 2005]), SOLAR 2000 (photoionization rate [Tobiska et al., 2000]), the
306 OMNI-2 time series (charge exchange with solar wind particles [King and Papitashvili,
307 2005]), and a model of the solar wind and radiation pressure latitude anisotropy [Bzowski,
308 2008]. We carried out the calculations for both spherically symmetric and latitude-
309 dependent solar wind structures following the approach proposed by Bzowski [2008],
310 who took into account (apart from the primary effects mentioned above) secondary
311 effects such as the Doppler dependence of the radiation pressure on the radial velocity of
312 the atoms due to the self-reversal of the solar Lyman-alpha line profile [Tarnopolski and
313 Bzowski, 2009], ionization by solar wind electrons [Bzowski et al., 2008], latitude
314 variation of the Lyman-alpha intensity [Auchere, 2005], and change of instantaneous
315 charge-exchange rate due to the change in relative velocity between the incoming ENA
316 and the expanding solar wind. The ecliptic 1 AU values of the relevant parameters are
317 shown in Figure 4. While there are a variety of short-duration fluctuations in these
318 parameters up to and including monthly (solar rotations) variations, the overall properties
319 are very similar over the intervals covering the first two sets of IBEX maps. One notable
320 exception is a solar wind event just before 2009.5, when a short, abrupt increase in solar
321 wind density (by a factor of ~6) occurred, resulting in a similar brief increase in the
322 charge-exchange rate.

323

324 Our model solar parameters as a function of heliolatitude are based on observations
325 obtained during the previous solar cycle [Bzowski et al., 2003; Bzowski, 2008]. Here we
326 calculate survival probabilities of H ENAs using this 3D model as well as validating the
327 3D results by comparing with a simpler 2D calculation where parameters do not depend
328 on heliolatitude. We examined the survival probabilities of H ENAs for the times and
329 geometry of IBEX observations used to construct the first two sets of IBEX maps for the
330 central energies of IBEX-Hi energy steps 2 through 6. Small latitude variations in
331 survival probability were obtained from the 3D calculation for ENAs approaching from
332 higher latitudes. Overall, however, the amplitude of latitudinal modulation due to
333 ionization (losses) of the ENAs in the supersonic solar wind are only a few percent and
334 thus have little impact on the IBEX maps.

335

336 We compared the survival probabilities for the time interval of the second set of IBEX
337 maps and calculated differences between the probabilities for the first and second sets of
338 maps. This comparison of survival probabilities shows that the effect on the survival
339 probabilities of violent and abrupt, but short-timed, events in the solar wind, such as the
340 event that happened shortly before 2009.5, is barely discernable. Figure 5 shows the
341 results of the 3D calculations where the ratio of survival probabilities is color coded as a
342 function of spacecraft spin phase and orbit number (from the second set of maps); ratios
343 for other energy steps are intermediate between the results shown here. The resulting
344 difference in survival probabilities between the equivalent orbits do not exceed 15% and

345 typically only ~5-10% for IBEX-Hi energy step 2 (the lowest one shown in this study).

346 For the rest of the higher-energy steps, these ratios are even smaller.

347

348 From our extensive calculations of these effects, we conclude that departures of

349 differences between the two sky maps of more than ~10% are most likely due to real

350 changes in the outer heliosphere and not modulation of ENAs propagating back through

351 the solar wind. In this study we chose to leave these corrections out of the IBEX data

352 being displayed in order to keep it as close as possible to the raw data and allow the

353 reader to independently assess the veracity of the temporal changes observed. One note of

354 caution for future studies of time variation is that the solar environment has been

355 unusually quiet since the start of IBEX observations. As the Sun becomes more active

356 and the solar wind more variable, these effects will become more significant and will

357 require the IBEX team to make explicit compensation or correction.

358

359 In contrast to the effects discussed above, we did need to make an explicit Compton-

360 Getting (CG) correction in order to quantitatively compare the first and second sets of

361 maps. This correction removes effects of the Earth's (and IBEX spacecraft's) ~30 km s⁻¹

362 motion around the Sun. The CG correction is important because IBEX maps are taken in

363 a way that the same swath of the sky is observed exactly six months apart, when IBEX

364 has the opposite orbital velocity around the Sun and therefore needs the opposite CG

365 correction. The methodology for making the CG correction was developed and validated

366 through a consensus process within the IBEX team; the resulting CG correction

367 methodology is described briefly in Appendix A with a more complete development and
368 discussion in *DeMajistre et al.* [2010].

369

370 Figure 6 compares the first (left column) and second (middle column) sets of CG-
371 corrected ENA flux maps. Because the maps are corrected to common energies, it is now
372 possible to combine them for improved statistics for studies that are not attempting to
373 examine time evolution. The right column shows these combined, exposure-time-
374 weighted, averaged maps of ENA flux over an entire year; these maps have reduced
375 statistical errors in some parts of the sky where the sampling times in one or both of the
376 individual maps were extremely limited. An interesting feature revealed in the combined
377 maps is the clear extension of the ribbon toward a complete ring compared to what can be
378 seen in the individual sets of sky maps. These combined maps are available to the broad
379 community, and owing to the better coverage and statistics, we recommend them over the
380 individual first and second sets of sky maps for testing hypotheses derived through theory
381 and modeling that are not directly addressing time variations in the ENA flux.

382

383 With CG-corrected maps and common color bars shown in Figure 6, it is clear that the
384 gross ENA emissions observed at the ribbon and underlying globally distributed flux are
385 extremely stable over the six-month interval between the first and second sets of sky
386 maps. In order to better identify and visualize small differences between the two sets of
387 maps, Figure 7 shows equirectangular projected maps of the first (left) and second
388 (middle) sets of IBEX sky maps, highlighting specific intensity levels with red and white
389 outlines as indicated by the red and white arrows on each color bar, respectively. These

390 contours help guide the eye in comparing specific quantitative flux levels. Again, the
391 overall ribbon and general structure appear to be highly similar, although now, some
392 smaller differences are also apparent.

393

394 The third column of Figure 7 shows difference maps at each energy, where we have
395 subtracted the flux in each pixel of the first sky maps from the flux in the equivalent pixel
396 of the second sky maps. Red indicates higher ENA fluxes in the second map compared to
397 the first, or increasing flux over the six months between observations; similarly, blue
398 indicates decreasing flux over these six months. Several artificial features are evident in
399 the regular sky maps and amplified in these difference maps. In particular, the rectangular
400 maps enable identification of vertical stripes that correspond to an apparent enhanced
401 ENA flux throughout the swath acquired over a single orbit. These result from an
402 abnormally high and mostly uniform background present during most of an orbit or an
403 orbit with poor statistics due to removal of time intervals of high background during an
404 orbit. These features are particularly evident over longitude ranges of $\sim 70^\circ$ to 90° and
405 $\sim 180^\circ$ to -150° .

406

407 Additionally, there is still a discontinuity in fluxes at angles of $\sim 0^\circ$ and $\sim 180^\circ$, where the
408 first (11 and 34) and last (33 and 56) orbits of each map abut each other. This was far
409 more significant in the uncorrected images (Figure 3) compared to the CG corrected ones
410 (Figure 6) showing that this correction has largely accounted for the differences in flux.
411 However, in the difference maps of Figure 7, one can still see a general redness in the
412 hemisphere between $\sim 0^\circ$ and $\sim 180^\circ$ and general blueness in the opposite hemisphere,

413 especially at lower latitudes and in the lower energies. This could represent a real change
414 in the globally distributed ENA flux being observed by IBEX, with increasing ENA
415 emissions from the nose and decreasing emissions from the tail between the two sets of
416 maps. However, because the discontinuity occurs at angles of $\sim 0^\circ$ and $\sim 180^\circ$, this
417 apparent difference is far more likely to be produced by imperfect CG correction of the
418 maps. A small systematic error in the CG correction (e.g., if there is still some residual
419 background noise in the lower-energy channels) will produce slight apparent asymmetries
420 between the ram and anti-ram viewing directions, especially at lower energies and
421 latitudes.

422

423 Notwithstanding the orbits with very low counting statistics and potentially imperfect CG
424 corrections, Figure 7 clearly shows some real differences between IBEX's first and
425 second sets of sky maps. First, both the north and south polar regions have reduced ENA
426 fluxes in the second map compared to the first, as evidenced by the blue across the top
427 and bottom of the difference maps. The effect appears to be a significant reduction in
428 ENA flux over the six months between the two maps. Because the magnitude of the CG
429 correction is smaller at the higher energies and decreases with increasing latitude
430 (becoming zero at the poles), it can not be responsible for this observed change.

431

432 Figure 8 shows a more quantitative analysis of the change in high-latitude flux between
433 the first and second sets of sky maps. Here, we calculated exposure-weighted fluxes and
434 associated uncertainties in 2° latitudinal bands by summing over all azimuths. We then
435 integrated these fluxes and their uncertainties starting at both poles and including

436 increasing numbers of lower latitudinal bands. Thus, for each latitude in Figure 8, the
437 flux and associated uncertainty represent integrations of ENA observations poleward of
438 that latitude and over all longitudes.

439

440 The results in Figure 8 are extremely consistent, with both poles showing significantly
441 lower fluxes (left column) in the second maps at the various energies separately and for
442 all energies combined (bottom panels). The right column provides accumulated
443 uncertainties as the integrations extend to lower latitudes. Uncertainties decrease with
444 integration over an increasing range of latitudes down from the poles and reach minima
445 ($\sim 25^\circ$ S and $\sim 15^\circ$ N from the poles – indicated by yellow regions) prior to growing as the
446 integrations start to include additional lower-latitude structure, such as the ribbon. By
447 using values around the uncertainty minima, this technique provides robust measures of
448 the differences in ENA flux from the two polar regions. Furthermore, the survival
449 probabilities are essentially identical for the polar regions, when integrated over all orbits
450 in the maps (see Figure 5). The overall reduction in flux at both poles is clear and
451 represents a decrease of ~ 10 - 15% over six months across the entire energy range from
452 ~ 0.5 - 6 keV.

453

454 A second small change that can be seen in the sets of sky maps in Figure 7 are some
455 detailed spatial variations and an apparent northward motion of the southern, nearly
456 horizontal (roughly fixed latitude) portion of the ribbon, between longitudes of $\sim 90^\circ$ –
457 180° . This shows up both in differences between the locations of the contours in the left
458 and center columns and in the difference maps as a characteristic combination of a

459 decreased (blue) region immediately southward of an increased (red) region; these two
460 indicators show up to a greater or lesser extent in all five energy channels shown. This
461 apparent motion is only one pixel ($\sim 6^\circ$), which is the angular resolution of the IBEX
462 sensors. Thus, while consistent differences over a large longitude range and multiple
463 energies are highly suggestive of a real, albeit small, temporal change in the overall ENA
464 emissions, this change can not be considered definitive.

465

466 The third difference between the first two sets of IBEX sky maps, on the other hand, is a
467 clear change in the “knot” region in the northern portion of the IBEX ribbon [McComas
468 *et al.*, 2009b; Funsten *et al.*, 2009a], which exhibits flux enhancements at higher energies
469 in the first sky maps. In the second set of maps, this knot is substantially diminished and
470 appears to spread out both to lower latitudes at the same longitude and to higher latitudes
471 at longitudes away from the nose. Figure 9 magnifies the region of the 2.7 keV maps
472 around the knot. Contours at the same flux levels help guide the eye for changes between
473 the maps and again in the difference image (bottom panel), blue indicates a reduction and
474 red an enhancement over the six months between the maps. Clearly the ENA emissions
475 from the small region of the knot are substantially reduced in the second maps.

476 Additionally, there is some evidence for enhanced emissions in the second maps both
477 poleward along the ribbon (upper left red region in the difference image) and southward
478 (lower right red region in the difference image), compared to the first. The overall
479 reduction in the knot emissions are substantial, with roughly one fourth to one third less
480 emission observed over six months.

481

482 As one final quantitative comparison between the two sets of sky maps, we divided the
483 maps into three contiguous regions as shown in Figure 10: 1) the *ribbon region*,
484 encapsulated in a shell of width $\pm 18^\circ$ centered at ecliptic coordinates of $221^\circ, 39^\circ$ as
485 found by *Funsten et al.* [2009a]; 2) The *nose and N pole region outside of the ribbon*; and
486 3) *the tail, flanks, and south pole region outside of the ribbon*. Table 2 provides the ratio
487 of exposure-weighted averaged fluxes in the second set of CG-corrected all-sky maps
488 compared to the first set ($6^\circ \times 6^\circ$ pixels) for each pair of full maps and for these three
489 regions separately. The fluxes are time-exposure-weighted values based on all pixels
490 within each region; errors are calculated from error propagation of the standard
491 deviations of the fluxes. The overall ENA fluxes are reduced in the second set of maps
492 compared to the first. The errors shown, however, do not include non-statistical errors,
493 such as residual, unsubtracted backgrounds. While small, these backgrounds can have a
494 substantial impact on the lower-energy channels (gray), the effects of which are further
495 amplified by the CG-correction process, which is highly sensitive to the energy spectrum.
496 On the other hand, the results in the top two energies (>2 keV) are less effected and
497 indicate small reductions in the ENAs measured by IBEX.

498

499 **3. Discussion**

500 New observations from IBEX provided in this study show that:

- 501 1) The globally distributed ENA fluxes from the outer heliosphere are extremely stable
- 502 over the six months between observations in the first two sets of IBEX sky maps;
- 503 2) The ribbon of enhanced ENA flux is also extremely stable over the interval between
- 504 the first two maps.

505 However, some statistically significant differences indicate that the outer heliosphere is
506 noticeably evolving over this short (six month) timeframe. In particular:

507 3) The overall ENA emissions observed by IBEX above ~ 2 keV appear to be slightly
508 lower in the second set of sky maps compared to the first both within the ribbon and
509 outside of it;

510 4) Both the north and south poles have significantly lower (~ 10 - 15%) ENA emissions in
511 the second set of sky maps compared to the first across the energy range from 0.5-6 keV;

512 5) The “knot” in the northern portion of the ribbon in the first maps is less intense and
513 appears to have spread and/or somewhat dissipated by the time the second set of maps
514 was acquired;

515 6) The detailed fluxes in the southern (horizontal) portion of the ribbon have evolved and
516 there may be a slight (one pixel, $\sim 6^\circ$) equatorward motion of its center.

517 The fact that both the globally distributed ENA flux and ENA emissions of the bright
518 ribbon are largely stable between IBEX’s first two sets of sky maps indicates a largely
519 stable heliospheric interaction and global configuration. It takes roughly one year for 1
520 keV solar wind to reach the TS at ~ 90 AU and then from half a year to nearly two years
521 for ENAs in the IBEX-Hi energy passbands to transit back ~ 100 AU from the inner
522 heliosheath (see Table 3); ENAs coming from the outer heliosheath, two to three times
523 further away take proportionally longer. Given the immense scale of the heliosphere and
524 its interstellar interaction, the many year time scales involved in plasma propagating
525 through this structure, and the anticipated long LOS integration paths producing ENAs in
526 the outer heliosphere, it would in fact have been far more surprising if the overall
527 structure was not largely stable for the short time of observations reported here. In future

528 studies, we plan to use time-lagged observations from various energies to reconstruct the
529 source fluxes in the outer heliosphere at fixed times in the past. Still, even with just the
530 first year of IBEX data, there are clear differences between the first two sets of maps,
531 indicating evolution of both globally distributed, and more localized, ribbon fluxes of
532 ENAs over only six months. Such variations likely indicate relatively thin source regions,
533 at least for the portions of the ENA emissions that are varying over this short timescale.

534
535 For the globally distributed flux, emissions from both polar regions were reduced by ~10-
536 15% over the six months between the first two maps. This reduction might be related to
537 decreasing solar wind flux over past several years [McComas et al., 2008] that should
538 decrease the density of the inner heliosheath. If these changes are caused by the evolution
539 of the global solar wind through the solar cycle then there may be as much as a factor of
540 two variation in ENA fluxes from the global heliosphere over the ~11-year solar cycle.
541 We note that the observation of polar evolution is a robust result because the CG
542 correction to the data is extremely small at the higher latitudes.

543

544 While it is possible that a second, apparent enhancement in the hemisphere toward the
545 nose (and reduction in the opposite hemisphere) could indicate real changes in the
546 globally distributed flux, such as an enhancement (decrease) in heliosheath thickness
547 and/or ion fluxes in nose (tail), we think it is far more likely that this apparent difference
548 is actually caused by an imperfect CG correction, which would have the largest effect at
549 the lowest energies and latitudes, as seen in the CG-corrected images.

550

551 In the ribbon, there are small but real variations between the maps, and thus time
552 evolution. The southern, horizontal portion of the ribbon appears to move northward
553 (toward the equator) possibly one pixel (6°), which is essentially the resolution of IBEX-
554 Hi. If this is actually a transverse motion of the source for this portion of the ribbon, then
555 for a source at ~ 100 AU, one pixel (6°) indicates a transverse speed of ~ 100 km s $^{-1}$; for a
556 source at ~ 250 AU, as suggested by the secondary ENA emission model (3), in the outer
557 heliosheath this would indicate a transverse speed of ~ 250 km s $^{-1}$. Finally, this apparent
558 equatorward motion is opposite to what would be expected for convection of structures
559 away from the nose either along the heliopause or in the inner or outer heliosheath.

560

561 As discussed above, the ribbon occupies a region where the interstellar magnetic field in
562 the outer heliosheath is roughly perpendicular to the LOS [McComas et al., 2009b]; this
563 is the region for which $\mathbf{B} \cdot \mathbf{r} \sim 0$, where \mathbf{B} is the interstellar magnetic field that is
564 compressed in the outer heliosheath as the interstellar flow deflects around the heliopause
565 [Schwadron et al., 2009]. In fact, the compression of the interstellar flow shifts the
566 location of the ribbon from a great circle (with angular radius of 90°) into an arc with an
567 angular radius of $<90^\circ$ [Funsten et al., 2009a]. We expect that greater compression and
568 deflection of interstellar flow near the nose causes the region of $\mathbf{B} \cdot \mathbf{r} \sim 0$ to decrease in
569 angular radius, therefore causing much of the ribbon to move equatorward, as observed.
570 This opens an important question about the potential for global changes in the properties
571 of the solar wind in the inner heliosheath to affect the deflection of interstellar flow
572 around the heliosphere, and therefore the location of the ribbon. For example, blunting of
573 the TS and heliopause, which may be related to a temporary (several year) reduction in

574 solar wind ram pressure, would lead to greater compression and deflection of interstellar
575 flow around the heliopause and, possibly, equatorward motion of the region where $\mathbf{B} \cdot \mathbf{r} \sim$
576 0.

577

578 The portion of the ribbon that shows clear time variation between the first two maps is
579 the knot in its northern region. Clearly, the brightest emissions at high energies in the first
580 set of sky maps are significantly diminished and spread out toward both higher and lower
581 latitudes; while the apparent spread northward and away from nose could be consistent
582 with convection away from nose, the southward enhancement is not. Evolution of the
583 knot indicates a spectral change, in which the flux in the central area of the knot has
584 become more like the adjacent sections of the ribbon and less like the most polar regions,
585 which all showed enhancements at the higher IBEX energies [Funsten et al., 2009a]. It is
586 interesting to consider if this change could be associated with the boundary between the
587 fast and slow solar wind regions moving and slower solar wind populating the inner
588 heliosheath at the latitude of the knot.

589

590 Given the largely stable structure, but clear evidence for evolution of at least some
591 portions of the ribbon, it is important to ask what the implications are for various
592 competing ideas about the source of the ribbon. Here we comment on each of the six
593 mechanisms suggested by McComas et al. [2009b] and discussed above, using the same
594 numbering system as in Figure 1:

595

596 (1) Maximum Pressure/Stagnation

597 In this explanation, the primary ribbon location should be generally stable owing to the
598 large-scale external pressure driver; however, changing internal pressure, for example
599 from small changes in the solar wind over time, could produce small changes in observed
600 ENA fluxes. Also, fine structure could be variable if produced by extrusions, which are
601 instabilities on the heliopause. Overall, based largely on the ribbon's general stability,
602 this explanation appears consistent with the observations.

603

604 (2) Primary ENAs from Compressions

605 This concept is similar to (1) in that the large-scale structure would be expected to be
606 largely stable since it comes from the external pressure, but fine structure should vary
607 since it is mostly driven by small-scale compressional instabilities in the draped ISM
608 field, most likely close to the heliopause. In this case, the ribbon would likely be less
609 sensitive to solar wind changes than (1), since the ENA production occurs in the outer
610 heliosheath instead of the inner heliosheath. However, the fact that the population is
611 highly suprathermal indicates that it may be produced, at least partially, by secondary
612 ENAs (3), in which case the population would be sensitive to changes in the solar wind.

613

614 (3) Secondary ENAs

615 The mechanism is related to (2), but solar wind and inner heliosheath ENAs produce ions
616 that become re-neutralized, so solar wind changes are probably more visible. Also, this
617 process should occur continuously over large distances along the LOS (ionization
618 lengths: ~550 AU beyond the heliopause at 1 keV and ~900 AU at 5 keV owing to scale
619 lengths of ionization via charge exchange assuming a 0.07 cm^{-3} LISM proton density).

620 With the need to accumulate emission over a length >550 to 900 AU, this model has
621 trouble producing significant variations over times as short as six months. For example,
622 at 1 keV a secondary ENA takes ~ 6 years to transit the 550 AU ionization length, and
623 therefore >12 years to move from the solar wind into the LISM, and then back into the
624 heliosphere where it can be detected. Finally, this mechanism doesn't produce fine
625 structure unless combined with (2), in which case it could be variable.

626

627 If the ribbon is formed outside the heliopause, then its location will shift with temporal
628 variations in ENA energies. The locus of sightlines that are perpendicular to the
629 interstellar magnetic field lines, $\mathbf{B} \cdot \mathbf{r} = 0$, varies with distance beyond the heliopause as
630 field lines bend around the heliosphere. The energy-dependent mean free paths of ENAs
631 therefore should affect the location of the ribbon's arc. The finite widths of the IBEX-Hi
632 energy channels (Table 1) translate into a range of mean-free paths represented by the
633 fluxes in a single channel (Table 2). For instance, the ionization length of ENAs in
634 energy step 3 range from 490 AU to 570 AU in a 0.074 /cc density plasma as appropriate
635 for the outer heliosheath. The nearly horizontal portion of the ribbon shifts northward by
636 approximately 0.7 degrees per 10 AU decrease in the mean-free path of an energy step 3
637 ENA, according to the heliosphere model in Schwadron et al. (2009), so this path
638 difference due to the channel width adds about six degrees to the ribbon width. This
639 sensitivity of the ribbon location to variations in the energy of the parent ion suggests that
640 comparisons between small shifts in the ribbon location and the time-lagged solar wind
641 properties may provide clues to the origin region of the ribbon.

642

643 (4) ENAs from magnetic reconnection at the heliopause

644 If the LISM field is stable over the times examined here and the solar wind's
645 interplanetary magnetic field paints the heliopause surface with alternating bands that are
646 only one solar rotation (26 days) wide [Suess et al., 2004], then the structure might be
647 expected to be narrowly banded (non-random) and moving away from the nose.
648 Generally speaking, the appearance of the $\sim 20^\circ$ -wide ribbon instead of numerous,
649 distributed source regions across the heliopause may seem inconsistent with this
650 explanation, although, if the reconnection was strongly organized by the pressure
651 maximum pushing the external and internal magnetic field together at the heliopause, this
652 might generate such a structure. Reconnection could produce time-variable patches
653 within the ribbon.

654

655 (5) ENAs from shock-accelerated pickup ions

656 A maximum pressure region could push in the TS locally to somehow trigger localized
657 production of pickup ions and subsequently enhanced ENA production. Since the TS
658 moves in and out and varies with the solar wind properties, this mechanism might be
659 expected to be the most variable over the solar cycle.

660

661 (6) ENAs from heliopause instabilities

662 This process should produce structures that always move away from the nose (assuming
663 it is the highest pressure region). For transverse speeds of $\sim 100 \text{ km s}^{-1}$, this would give
664 $\sim 6^\circ$ (one pixel) per six months. This is about the rate of the possible motion of the
665 southern portion of the ribbon; however, if that portion of the ribbon did move, it

666 appeared to move toward the nose and not away from it, as the mechanism would suggest.

667 Finally, this process could produce fine scale structures, which would vary over time, but

668 it would likely move away from the nose also.

669

670 For the seventh mechanism suggested by *Grzedzielski et al.* [2010], any variations on

671 such short timescales seem problematic for ENAs produced by charge exchange between

672 neutral H atoms at the nearby edge of the LIC and hot protons from the Local Bubble

673 owing to the immense scale of this interaction. On the other hand, even if this mechanism

674 is operating, the ENA flux observed by IBEX likely derives from a combination of

675 sources including a more “local” heliospheric one, which could account for observed

676 temporal variations.

677

678 The IBEX mission continues to provide a wealth of new information about the outer

679 heliosphere and its interaction with the LISM. This overall interaction appears to be

680 evolving over time, most likely as the solar wind evolves over the solar cycle.

681 Observations from IBEX are continuing and each roughly week-long orbit returns

682 another swath of the sky, building up new sets of sky maps each six months. While the

683 mission was designed and originally slated to last only two years, the IBEX Team used

684 some of the spacecraft’s remaining hydrazine after launch to quickly raise the orbit

685 perigee and reduce the radiation fluence from passing through the Earth’s radiation belts.

686 Thus, with a little luck, IBEX will continue its remarkable mission of discovery and

687 exploration for many years to come, allowing us to sample the outer heliospheric ENAs

688 over the solar cycle.

689

690 Acknowledgements. We thank E.C. Roelof for work on the CG effect and are deeply
691 indebted to all of the outstanding men and women who have made the IBEX mission
692 such a wonderful success. This work was carried out as a part of the IBEX project, with
693 support from NASA's Explorer Program and Polish Ministry for Science and Higher
694 Education grant NS-1260-11-09.

695

696 **Appendix A: Compton-Getting Correction of the Data**

697

698 The IBEX spacecraft moves around the Sun with a velocity that is a measurable fraction
699 of the velocity of the ENAs being measured. Therefore, a Compton-Getting correction is
700 needed to quantitatively compare measurements taken at different parts of the year. The
701 first two six-month maps are transformed from the spacecraft reference frame into the
702 inertial reference frame at the central energy of each of the highest five instrument energy
703 steps (0.71, 1.11, 1.74, 2.73, and 4.29 keV). The Earth's orbital velocity is $\sim 30 \text{ km s}^{-1}$,
704 which is nearly 7% of the velocity of a 1 keV H atom (the orbital velocity of IBEX
705 around the Earth is $\sim 1 \text{ km s}^{-1}$ and will be neglected here). Figure A1 shows the change in
706 angle and energy for the transformation of an ENA from a fixed energy in the spacecraft
707 frame to the inertial reference frame. The change in angle and energy depend on the
708 central look direction of the sensor as it rotates about the spin axis directed approximately
709 toward the Sun. In general, the effects associated with the change in reference frame
710 become most important at the lowest energy steps observed by IBEX, and the corrections

711 are relatively small ($<5^\circ$ change in angle, and $<15\%$ change in energy) at the energies
712 analyzed here (>0.7 keV).

713

714 The reference frame changes in energy and angle are particularly important when
715 comparing sky maps obtained six months apart, since each map is derived from opposite
716 halves of the year, and thus opposing orbital velocity directions. For example, in Figure 2
717 we see that the nose of the heliosphere is imaged in March. Since the orbital velocity and
718 actual velocity of the particle are added in the observation, the apparent velocity of the
719 ENAs from the nose direction is larger in the IBEX spacecraft's frame of reference. That
720 is, IBEX will effectively sample lower-energy heliospheric ENAs from the nose. Six
721 months later, in September, the nose is again imaged, but this time in the wake direction
722 (opposed to the velocity vector), so IBEX effectively samples higher-energy heliospheric
723 ENAs at the same energy step. In order to compare maps taken six months apart we must
724 correct for the difference in effective sampling energy in the two maps. This Appendix
725 describes the correction implemented in the IBEX data analysis. It is worth noting that
726 this particular correction methodology was vetted through a consensus process with the
727 IBEX Science Team, which included significant testing and validation.

728

729 Let \mathbf{v} be the velocity vector of an ENA in the IBEX frame. The IBEX spacecraft moves
730 with the velocity \mathbf{u}_{SC} with respect to the solar inertial frame. The velocity vector of the
731 ENA in the solar inertial frame, \mathbf{v}_i , is therefore $\mathbf{v}_i = \mathbf{v} + \mathbf{u}_{SC}$. IBEX measures ENAs in a
732 plane nearly perpendicular to the direction of the Sun and the ENA incidence velocity
733 angle, θ , is the incoming velocity angle of the ENA referenced to Ecliptic North in right-

734 handed rotation about the sunward axis (Z). Note that the incidence velocity angle, θ ,
 735 represents the angle of an incoming ENA, which has velocity, $-\mathbf{v}$. We represent vectors
 736 in a coordinate system where the X axis points towards the North Ecliptic Pole (NEP),
 737 the Y axis points in the direction of Earth's motion about the Sun (these are Z_{GSE} and $-$
 738 Y_{GSE} , respectively), and the Z axis is directed toward the Sun. With this representation,
 739 Galilean transformations are explicitly

$$740 \quad v \begin{vmatrix} \cos \theta \\ \sin \theta \end{vmatrix} = v_i \begin{vmatrix} \cos \theta_i \\ \sin \theta_i \end{vmatrix} + \begin{vmatrix} 0 \\ u_{SC} \end{vmatrix} \quad (\text{A1})$$

741
 742 The magnitude of the velocity in the inertial frame is therefore

$$744 \quad v_i = v \sqrt{1 - 2 \left(\frac{u_{SC}}{v} \right) \sin \theta + \left(\frac{u_{SC}}{v} \right)^2} \quad (\text{A2})$$

745
 746 the angular aberration between the systems is

$$747 \quad \begin{aligned} \cos \theta_i &= \frac{v}{v_i} \cos \theta \\ \sin \theta_i &= \frac{v}{v_i} \sin \theta - \frac{u_{SC}}{v_i} \end{aligned} \quad (\text{A3})$$

748
 749 and the ratio of the energies is

$$751 \quad \frac{E_i}{E} = \frac{\mathbf{v}_i \cdot \mathbf{v}_i}{\mathbf{v} \cdot \mathbf{v}} = 1 - 2 \frac{u_{SC}}{v} \sin \theta + \left(\frac{u_{SC}}{v} \right)^2 \quad (\text{A4})$$

752
 753 The invariance of phase-space density requires that the ENA flux in the solar inertial
 754 frame, $j_i(\theta_i, E_i)$, be related to the ENA flux in the IBEX spacecraft frame, $j(\theta, E)$, as

$$755 \quad j_i(\theta_i, E_i) = \frac{E_i}{E} j(\theta, E) \quad (\text{A5})$$

756
 757 which, along with the equations above, allows us to express the ENA flux in the solar
 758 inertial frame given measured fluxes in the IBEX frame. It is important to note, however,
 759 that for measurements at a fixed energy and a regular-angle grid, the resulting fluxes in

760 the solar inertial frame will be given at multiple energies on an irregular-angular grid.
 761 This is rather awkward for producing maps and makes comparison of maps taken six
 762 months apart difficult. We therefore develop a method that allows us to produce estimates
 763 of the flux in the solar inertial frame at fixed energies and on a regular angle grid
 764
 765 Fluxes at a fixed energy in the solar inertial frame will require us to estimate fluxes in the
 766 IBEX frame at various energies. Given a spectrum of measured fluxes at the nominal
 767 IBEX channel energies, $j_n=j(\theta, E_n)$, we can estimate the flux at nearby energies using the
 768 log-log Taylor expansion from

$$769 \quad \ln j_{est}(\theta, E) = \ln j_n + k_n \ln \frac{E}{E_n} + \frac{a_n}{2} \left(\ln \frac{E}{E_n} \right)^2 + O \left[\left(\ln \frac{E}{E_n} \right)^3 \right] \quad (A6)$$

770 where the derivatives of the spectrum
 771

$$773 \quad k_n = \left. \frac{\partial \ln j}{\partial \ln E} \right|_{E_n}, a_n = \left. \frac{\partial^2 \ln j}{\partial (\ln E)^2} \right|_{E_n} \quad (A7)$$

774
 775 are determined numerically from the measured spectrum. For convenience, we calculate
 776 the fluxes in the solar inertial frame at the nominal channel energies, E_n , and therefore
 777 write

$$778 \quad j_i(\theta_i, E_n) = \frac{E_n}{E} j_{est}(\theta, E) \quad (A8)$$

779 where the variable energy, E , is determined by the ratios of the energies written above
 780
 781 (A4).

782
 783 In practice, we first calculate the required energy in the IBEX frame using (A4), then
 784 determine the fluxes in the solar inertial frame using (A6) and (A8). Note that (A8) is

785 given on the irregular angular grid, θ_i . We then use a simple linear interpolation to re-grid
786 these results back to the measurement grid, θ . We have therefore transformed
787 measurements of fluxes in the IBEX measurement frame into the solar inertial frame at
788 fixed energies on a regular-angle grid, the results of which allow us to compare maps
789 taken six months apart. A more complete development and discussion of how we correct
790 for the CG effect in IBEX data can be found in *DeMajistre et al.* [2010].

791

792 **References**

793

794 Auchère, F., J. W. Cook, J. S. Newmark, D. R. McMullin, R. von Steiger, and M. Witte
795 (2005), The Heliospheric He II 30.4 nm Solar Flux During Cycle 23, *Astrophys. J.*,
796 625(2), 036-1044, doi:10.1086/429869.

797 Borovikov, S. N., N. V. Pogorelov, G. P. Zank, and I. A. Kryukov (2008), Consequences
798 of the Heliopause Instability Caused by Charge Exchange, *Astrophys. J.*, 682(2),
799 1404-1415, doi:10.1086/589634.

800 Burlaga, L. F., N. F. Ness, and M. H. Acuna, Multiscale structure of magnetic fields in
801 the heliosheath (2006), *J. Geophys. Res.*, 111, A09112, doi:10.1029/2006JA011850.

802 Bzowski, M. (2008), Survival probability and energy modification of hydrogen energetic
803 neutral atoms on their way from the termination shock to Earth orbit, *Astron.*
804 *Astrophys.*, 488(3), 1057-1068, doi: 10.1051/0004-6361:200809393.

805 Bzowski, M., Moebius, E., Tarnopolski, S., Izmodenov, V., Gloeckler, G., Density of
806 neutral interstellar hydrogen at the termination shock from Ulysses pickup ion
807 observations", *A&A*, v. 491, pp 7-19, 2008.

- 808 Chalov, S. V. and H. J. Fahr (1996), A three-fluid model of the solar wind termination
809 shock including a continuous production of anomalous cosmic rays, *Astron.*
810 *Astrophys.*, 311, 317-328.
- 811 Chalov, S.V., D. B. Alexashov, D. McComas, V. V. Izmodenov, Y. G. Malama, and N.
812 Schwadron (2010, in press), Scatter-free pickup ions beyond the heliopause as a
813 model for the Interstellar Boundary Explorer (IBEX) ribbon, *Astrophys. J.*
- 814 DeMajistre, R., E. C. Roelof, M. Gruntman, G. Crew, E. Christian, M. Lee, E. Moebius,
815 T. Moore, N. Schwadron, and D.J. McComas (2010, preparation), Velocity Corrected
816 Energetic Neutral Atom Spectra from the Outer Heliosphere.
- 817 Fahr, H.-J., I. V. Chashei, and D. Verscharen (2009), Injection to the pick-up ion regime
818 from high energies and induced ion power-laws, *Astron. Astrophys.*, 505, 329–337
819 doi: 10.1051/0004-6361/200810755.
- 820 Funsten, H. O., F. Allegrini, G. B. Crew, R. DeMajistre, P. C. Frisch, S. A. Fuselier, M.
821 Gruntman, M., P. Janzen, D. J. McComas, E. Möbius, B. Randol, D. B. Reisenfeld, E.
822 C. Roelof, and N. Schwadron (2009a), Structures and spectral variations of the outer
823 heliosphere in IBEX energetic neutral atom maps, *Science*, 326(5955), 964-966,
824 doi:10.1126/science.1180927.
- 825 Funsten, H.O., F. Allegrini, P. Bochsler, G. Dunn, S. Ellis, D. Everett, M. J. Fagan, S.A.
826 Fuselier, M. Granoff, M. Gruntman, A. A. Guthrie, J. Hanley, R.W. Harper, D.
827 Heirtzler, P. Janzen, K. H. Kihara, B. King, H. Kucharek, M. P. Manzo, M. Maple, K.
828 Mashburn, D. J. McComas, E. Moebius, J. Nolin, D. Piazza, S. Pope, D. B.
829 Reisenfeld, B. Rodriguez, E. C. Roelof, L. Saul, S. Turco, P. Valek, S. Weidner, P.
830 Wurz, and S. Zaffke (2009b), The Interstellar Boundary Explorer High Energy

831 (IBEX-Hi) neutral atom imager, *Space Sci. Rev.*, 146, 75-103, doi:10.1007/s11214-
832 009-9504-y.

833 Fuselier, S. A., F. Allegrini, H. O. Funsten, A. G. Ghielmetti, D. Heirtzler, H. Kucharek,
834 O. W. Lennartsson, D. J. McComas, E. Möbius, T. E. Moore, S. M. Petrinec, L. A.
835 Saul, J. A. Scheer, N. Schwadron, and P. Wurz (2009), Width and variation of the
836 ENA flux ribbon observed by the Interstellar Boundary Explorer, *Science*, 326(5955),
837 doi: 10.1126/science.1180981, 962-964.

838 Grzedzielski, S., M. Bzowski, A. Czechowski, H.O. Funsten, D.J. McComas, and N.A.
839 Schwadron, (2010, submitted) A Possible generation mechanism for the IBEX ribbon
840 from outside the heliosphere, *Astrophys. J.*

841 Gurnett, D. A., W. S. Kurth, I. H. Cairns, and J. Mitchell (2006), The local interstellar
842 magnetic field direction from direction-finding measurements of heliospheric 2-3 kHz
843 radio emissions, 5th Annual IGPP International Astrophysics Conference, AIP
844 Conference Proceedings, 858, 29-134, doi:10.1063/1.2359317

845 Heerikhuisen, J., N. V. Pogorelov, G. P. Zank, G. B. Crew, P. C. Frisch, H. O. Funsten, P.
846 H. Janzen, D. J. McComas, D. B. Reisenfeld, and N. A. Schwadron (2010), Pick-Up
847 Ions in the Outer Heliosheath: A Possible Mechanism for the Interstellar Boundary
848 EXplorer Ribbon, *Astrophys. J. Letters*, doi:10.1088/2041-8205/708/2/L126.

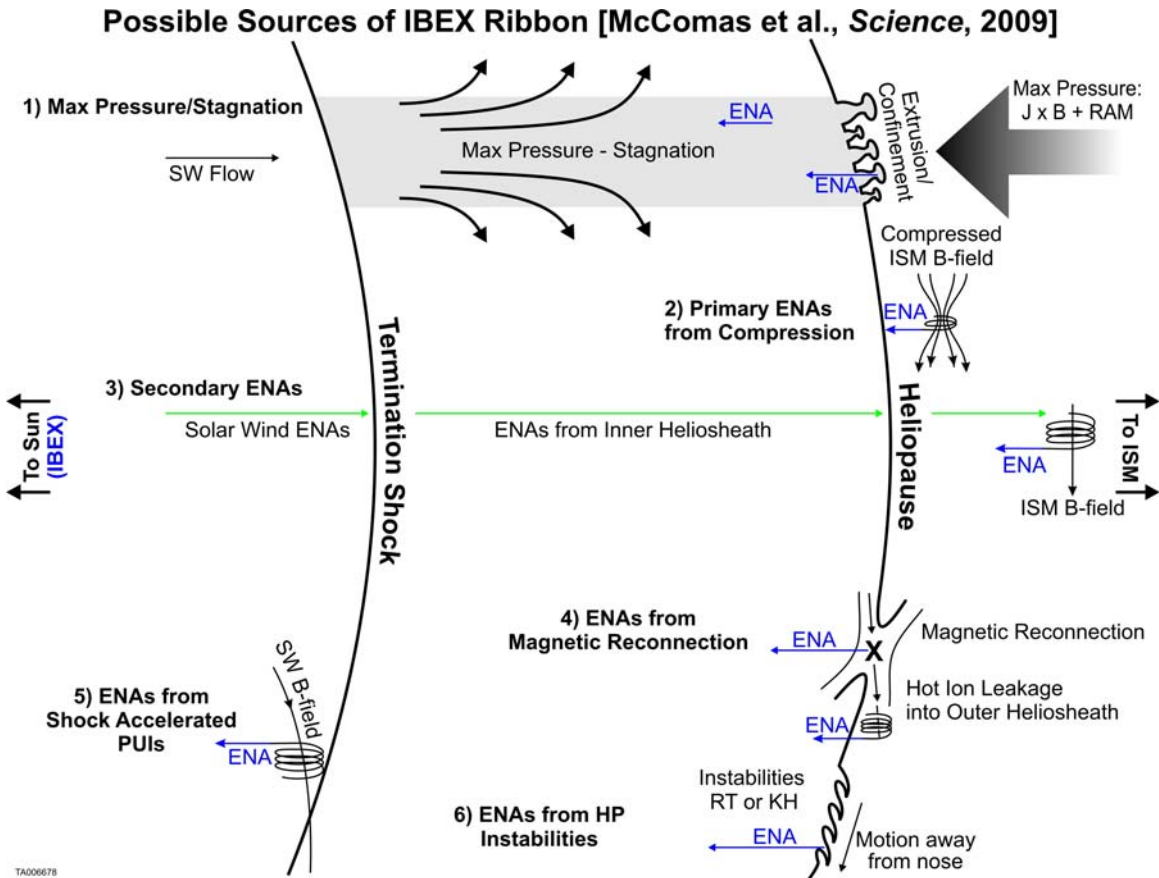
849 Izmodenov, V. V., Y. G. Malama, M. S. Ruderman, S. V. Chalov, D. B. Alexashov, O. A.
850 Katushkina, and E. A. Provornikova (2009), Kinetic-gasdynamic modeling of the
851 heliospheric interface, *Space Sci. Rev.*, 146(1-4), 329-351, doi:10.1007/s11214-009-
852 9528-3.

- 853 King, J. H., and N. E. Papitashvili (2005), Solar wind spatial scales in and comparisons of
854 hourly Wind and ACE plasma and magnetic field data, *J. Geophys. Res.*, 110(A2),
855 A02104, doi:10.1029/2004JA010649.
- 856 Krimigis, S. M., D. G. Mitchell, E. C. Roelof, K. C. Hsieh, and D. J. McComas (2009),
857 Imaging the interaction of the heliosphere with the interstellar medium from Saturn
858 with Cassini, *Science*, 326(5955), 971-973, doi:10.1126/science.1181079.
- 859 Lallement, R., E. Quémerais, J. L. Bertaux, S. Ferron, D. Koutroumpa, R. Pellinen (2005),
860 Deflection of the interstellar neutral hydrogen flow across the heliospheric interface,
861 *Science*, 307(5714), 1447-1449, doi:10.1126/science.1107953.
- 862 McComas, D. J., R. W. Ebert, H. A. Elliott, B. E. Goldstein, B. E., J. T. Gosling, N. A.
863 Schwadron, and R. M. Skoug (2008), Weaker Solar Wind from the Polar Coronal
864 Holes and the Whole Sun, *Geophys. Res. Lett.*, 35(18), L18103,
865 doi:10.1029/2008GL034896.
- 866 McComas, D.J., F. Allegrini, F., P. Bochsler, M. Bzowski, M. Collier, H. Fahr, H.
867 Fichtner, P. Frisch, H. O. Funsten, S. A. Fuselier, G. Gloeckler, M. Gruntman, V.
868 Izmodenov, P. Knappenberger, M. Lee, S. Livi, D. Mitchell, E. Möbius, T. Moore, S.
869 Pope, D. Reisenfeld, E. Roelof, J. Scherrer, N. Schwadron, R. Tyler, M. Wieser, M.
870 Witte, P. Wurz, and G. Zank (2009a), IBEX – Interstellar Boundary Explorer, *Space*
871 *Sci. Rev.*, 146(1-4), 11-33, doi:10.1007/s11214-009-9499-4.
- 872 McComas, D. J., F. Allegrini, P. Bochsler, M. Bzowski, E. R. Christian, G. B. Crew, R.
873 DeMajistre, H. Fahr, H. Fichtner, P. C. Frisch, H. O. Funsten, S. A. Fuselier, G.
874 Gloeckler, M. Gruntman, J. Heerikhuisen, V. Izmodenov, P. Janzen, P.
875 Knappenberger, S. Krimigis, H. Kucharek, M. Lee, G. Livadiotis, S. Livi, R. J.

- 876 MacDowall, D. Mitchell, E. Möbius, T. Moore, N. V. Pogorelov, D. Reisenfeld, E.
877 Roelof, L. Saul, N. A. Schwadron, P. W. Valek, R. Vanderspek, P. Wurz, and G. P.
878 Zank (2009b), Global observations of the interstellar interaction from the Interstellar
879 Boundary Explorer (IBEX), *Science*, 326(5955), 959-962,
880 doi:10.1126/science.1180906.
- 881 Möbius, E., P. Bochsler, M. Bzowski, G. B. Crew, H. O. Funsten, S. A. Fuselier, A.
882 Ghielmetti, D. Heirtzler, V. V. Izmodenov, M. Kubiak, H. Kucharek, M. A. Lee, T.
883 Leonard, D. J. McComas, L. Petersen, L. Saul, J. A. Scheer, N. Schwadron, M. Witte,
884 and P. Wurz, (2009), Direct observations of interstellar H, He, and O by the
885 Interstellar Boundary Explorer, *Science*, 326(5955), 969-971,
886 doi:10.1126/science.1180971.
- 887 Pogorelov, N. V., J. Heerikhuisen, J. J. Mitchell, I. H. Cairns, and G. P. Zank (2009),
888 Heliospheric asymmetries and 2-3 kHz radio emission under strong interstellar
889 magnetic field conditions, *Astrophys. J.*, 695(1), L31-L34, doi:10.1088/0004-
890 637X/695/1/L31.
- 891 Prested, C., N. Schwadron, J. Passuite, B. Randol, B. Stuart, G. Crew, J. Heerikhuisen, N.
892 Pogorelov, G. Zank, M. Opher, F. Allegrini, D. J. McComas, M. Reno, E. Roelof, S.
893 Fuselier, H. Funsten, E. Moebius, and L. Saul (2008), Implications of solar wind
894 suprathermal tails for IBEX ENA images of the heliosheath, *J. Geophys. Res.*,
895 113(A6), A06102, doi:10.1029/2007JA012758.
- 896 Richardson, J. D., J. C. Kasper, C. Wang, J. W. Belcher, and A.J. Lazarus (2008), Cool
897 heliosheath plasma and deceleration of the upstream solar wind at the termination
898 shock, *Nature*, 454(7200), 63-66, doi:10.1038/nature07024.

- 899 Richardson, J. D., E. C. Stone, J. C. Kasper, J. W. Belcher, R. B. Decker (2009), Plasma
900 flows in the heliosheath, *Geophys. Res. Lett.*, 36(10), L10102,
901 doi:10.1029/2009GL038421.
- 902 Schwadron, N. A., M. Bzowski, G. B. Crew, M. Gruntman, H. Fahr, H. Fichtner, P. C.
903 Frisch, H. O. Funsten, S. Fuselier, J. Heerikhuisen, V. Izmodenov, H. Kucharek, M.
904 Lee, G. Livadiotis, D. J. McComas, E. Moebius, T. Moore, J. Mukherjee, N. V.
905 Pogorelov, C. Prested, D. Reisenfeld, E. Roelof, and G. P. Zank (2009), Comparison
906 of Interstellar Boundary Explorer observations with 3D global heliospheric models,
907 *Science*, 326(5955), 966-968, doi:10.1126/science.1180986.
- 908 Slavin, J. D., and P. C. Frisch, The boundary conditions of the heliosphere:
909 photoionization models constrained by interstellar and in situ data, *Astron. Astrophys.*
910 491(1), 53-68, doi:10.1051/0004-6361:20078101.
- 911 Stone, E. C. (2008), An asymmetric solar wind termination shock, *Nature*, 454(7200),
912 71-74, doi:10.1038/nature07022.
- 913 Suess, S.T. (2004), The magnetic field in the outer heliosphere, *Physics of the Outer*
914 *Heliosphere: Third International IGPP Conference*, 719, 10-15,
915 doi:10.1063/1.1809492.
- 916 Tarnopolski, S., and M. Bzowski (2009), Neutral interstellar hydrogen in the inner
917 heliosphere under the influence of wavelength-dependent solar radiation pressure,
918 *Astron. Astrophys.*, 493(1), 207-216, doi:10.1051/0004-6361:20077058.
- 919 Tobiska, W. K., T. Woods, F. Eparvier, R. Viereck, L. Floyd, D. Bouwer, G. Rottman,
920 and O. R. White (2000), The SOLAR2000 empirical solar irradiance model and

- 921 forecast tool, *J. Atmos. Sol. Terr. Phys.*, 62(14), 1233-1250, doi:10.1016/S1364-
922 6826(00)00070-5.
- 923 Woods, T. N., F. G. Eparvier, S. M. Bailey, P. C. Chamberlin, J. Lan, G. J. Rottman, S. C.
924 Solomon, W. K. Tobiska, and D. L. Woodraska (2005), Solar EUV Experiment
925 (SEE): Mission overview and first results, *J. Geophys. Res.*, 110(A1), A01312,
926 10.1029/2004JA010765.
- 927 Zank, G. P., J. Heerikhuisen, N. V Pogorelov, R. Burrows, D. McComas
928 (2010), Microstructure of the Heliospheric Termination Shock: Implications for
929 Energetic Neutral Atom Observations, *Astrophys. J.*, 708(2), 1092-1106.
- 930 Zank, G. P., H. L. Pauls, I. H. Cairns, G. M. Webb (1996), Interstellar pickup ions and
931 quasi-perpendicular shocks: Implications for the termination shock and
932 interplanetary shocks, *J. Geophys. Res.*, 101(A1), 457-478.
- 933



934

935

Figure 1. Schematic diagram summarizing the six possible sources of the ribbon of

936

enhanced ENA emissions in the IBEX data identified by McComas et al. [2009b]. These

937

comprise: (1) ENAs produced in a region of maximum pressure and stagnation in the

938

inner heliosheath, possibly producing extrusions of the heliopause; (2) ENAs

939

preferentially produced with $\sim 90^\circ$ pitch angles through localized compression of the very

940

local interstellar magnetic field outside the heliopause; (3) Secondary ENAs produced by

941

ionization and subsequent reemission of outward traveling ENAs from the solar wind and

942

pickup ions inside the termination shock and/or from the inner heliosheath; (4) ENAs

943

produced in association with magnetic reconnection across the heliopause; (5) ENAs

944

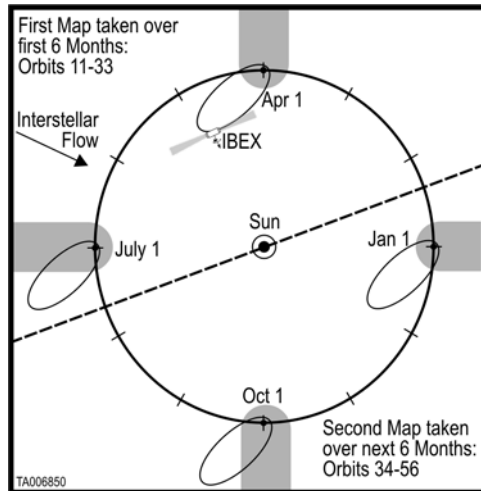
produced from shock accelerated ions just upstream and downstream of the termination

945

shock; and (6) ENAs produced in enhanced localized regions at the heliopause, owing to

946

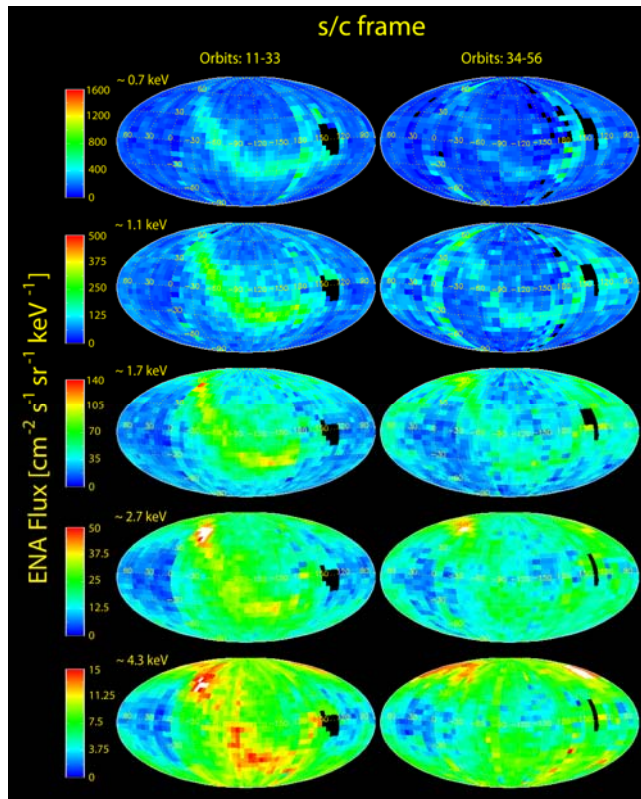
the development of Rayleigh–Taylor and/or Kelvin–Helmholtz instabilities



947

948 *Figure 2. Schematic diagram of IBEX orbital geometry showing the inertially fixed IBEX*
949 *orbit with respect to the Earth and magnetosphere (gray) over the year. The IBEX*
950 *spacecraft is repointed once each orbit and views perpendicular to its Sun-pointing spin*
951 *axis. The first and second maps were taken over separate halves of the Earth's orbit, with*
952 *IBEX's apogee being mostly sunward of the Earth for the first maps and tailward for the*
953 *second.*

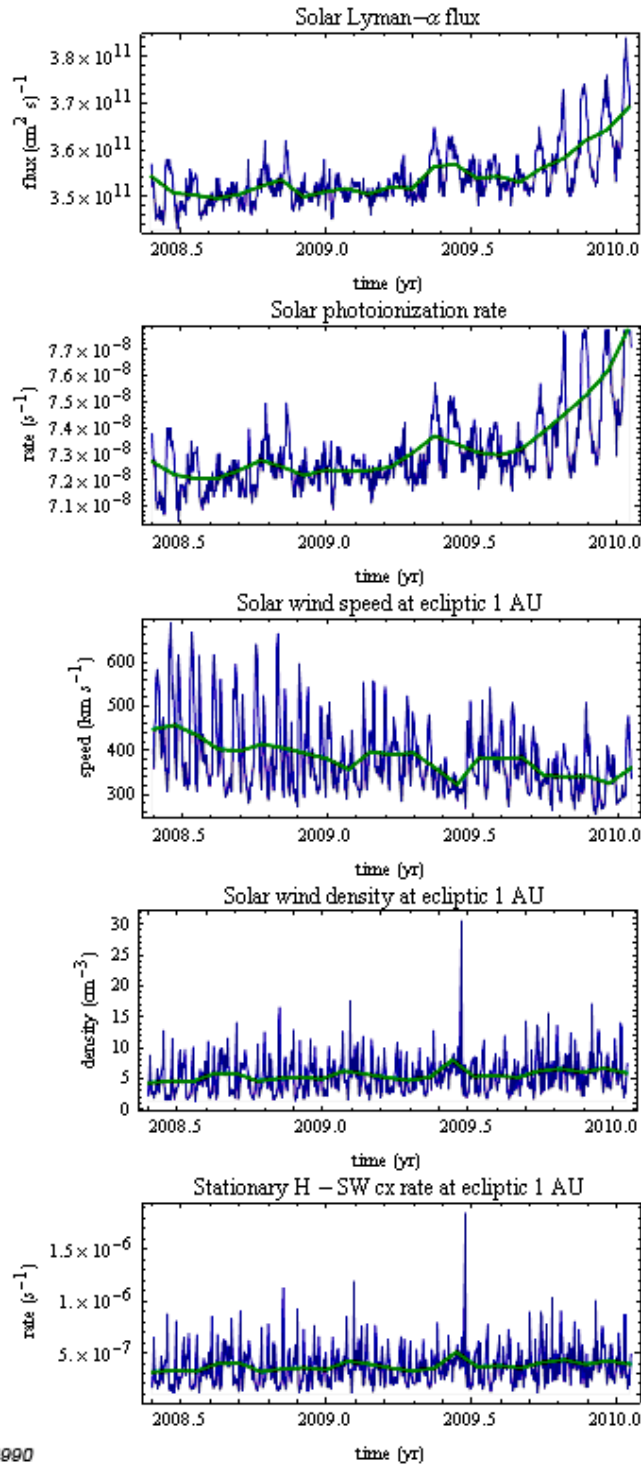
954



955

956 *Figure 3. IBEX-Hi observations showing the first (left) and second (right) sets of all-sky*
957 *maps in spacecraft coordinates. Both sets of maps show similar fluxes and the existence*
958 *of the ribbon of enhanced emissions. The maps are shown in Mollweide projections with*
959 *the nose of the heliosphere in the center of each map and the tail at both the far left and*
960 *far right; angles are given in ecliptic J-2000 latitude and longitude.*

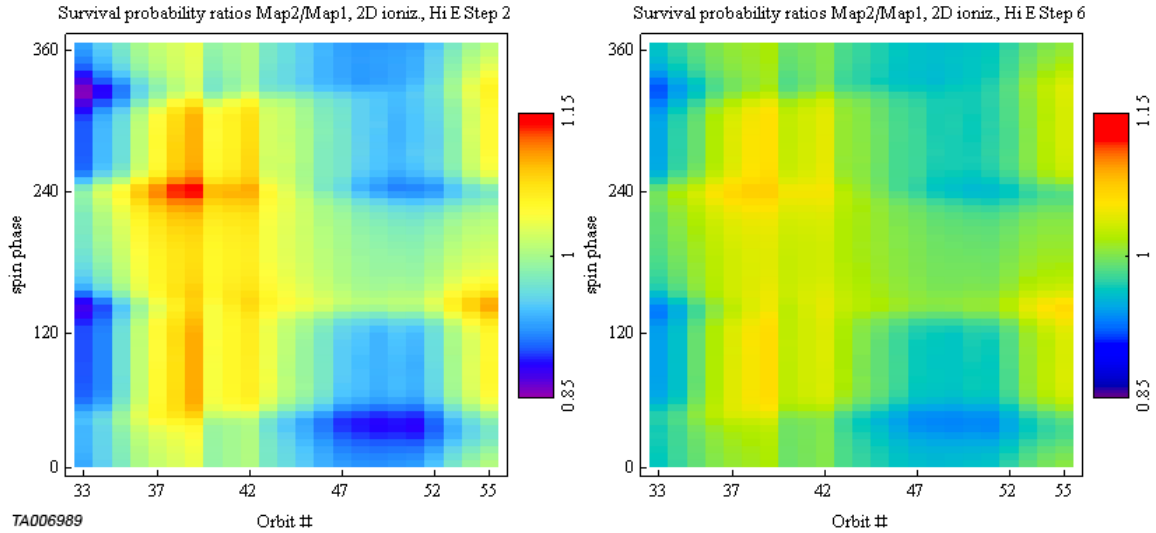
961



962 TA006990

963 Figure 4. Daily (thin blue lines) and running 27-day averages (thick green lines) of solar
964 radiation and solar wind parameters relevant for calculating ionization rates of H ENAs
965 observed by IBEX (see text).

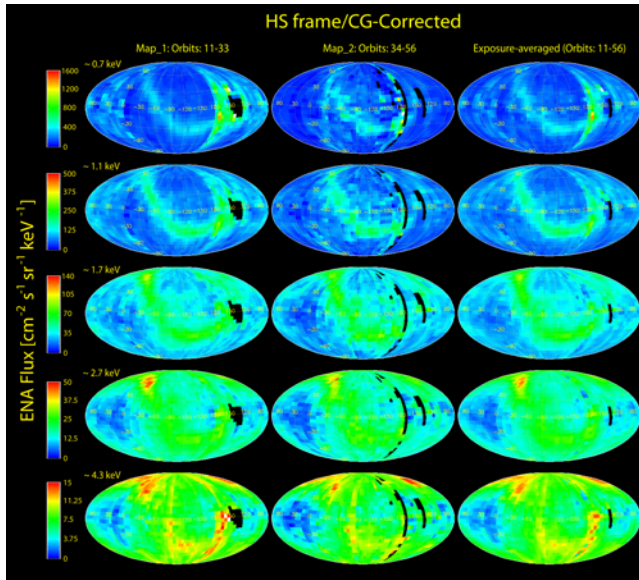
966



967

968 *Figure 5. Calculated ratios of the survival probabilities of H ENAs in the second set of*
969 *sky maps divided by they survival probabilities in the first map for IBEX-Hi energy steps*
970 *2 (left) and 6 (right) as a function of spin phase vs orbit number (for the second map).*
971 *Ratios for energy steps 3-5 become progressively smaller between these two extremes.*
972 *Overall, survival probabilities are generally only a few percent different between the two*
973 *sets of maps, especially at higher energies.*

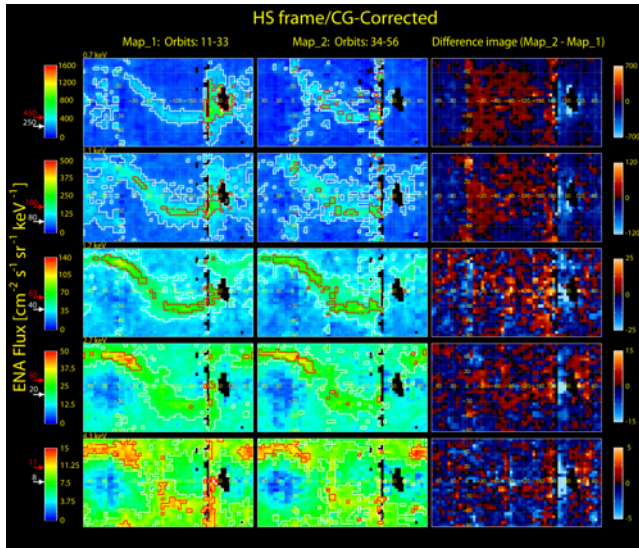
974



975

976 *Figure 6. Compton-Getting corrected ENA fluxes for the first (left), second (middle), and*
977 *combined (right) sets of all-sky maps from IBEX. While the second maps are somewhat*
978 *noisier, the common color bar for each energy range allows for rapid quantitative*
979 *comparison. The maps clearly show similar structures and fluxes, although some*
980 *statistically significant differences are observed.*

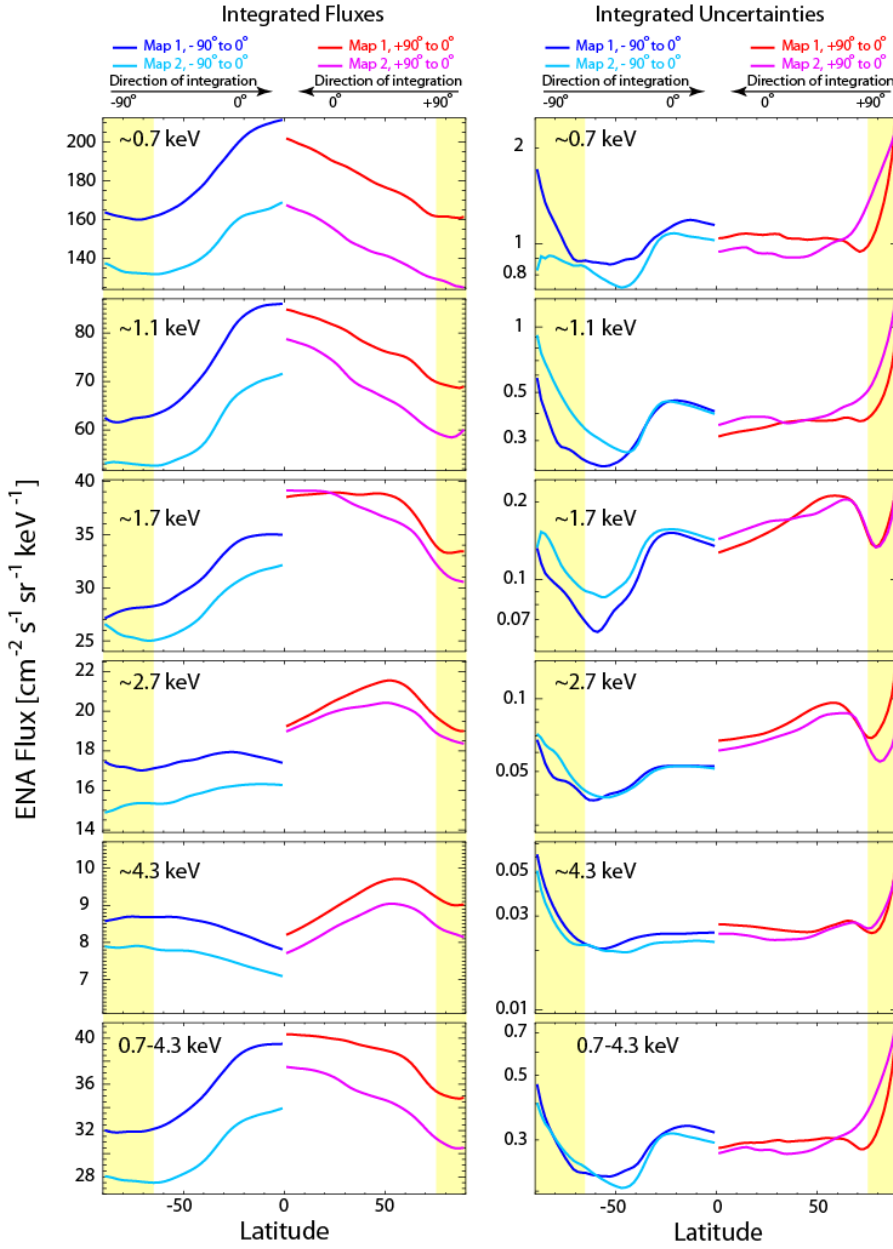
981



982

983 *Figure 7. Equirectangular projections of CG-corrected first (left) and second (middle)*
984 *sets of IBEX all-sky maps with specific contours (red and white outlines with values*
985 *indicated by arrows next to color bars) to help guide the eye. The right column of panels*
986 *show difference images where red (blue) indicates more (less) flux in the second map*
987 *compared to the first.*

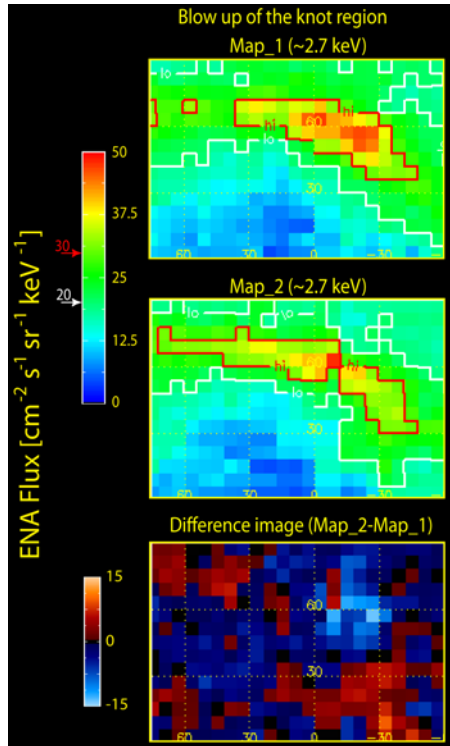
988



989

990 *Figure 8. Quantitative comparison of ENA fluxes from the south (blues) and north (reds)*
 991 *between IBEX's first (dark blue and red) and second (light blue and purple), sky maps*
 992 *using 2° resolution. The left column shows the difference in integrated CG-corrected flux*
 993 *for each of the energy steps (and all steps summed – bottom), while the right column*
 994 *shows the overall uncertainty of the integrated flux (see text); yellow-shaded regions*
 995 *highlight the polar regions.*

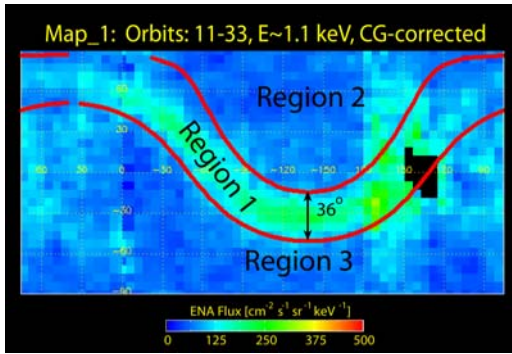
996



997

998 *Figure 9. Blow up of the knot region in the northern part of the ribbon in map 1 (top) and*
999 *2 (middle) at ~2.7 keV. The bottom panel shows the difference image of this region for all*
1000 *pixels. Clearly, the knot emissions have significantly diminished (and possibly spread*
1001 *out) between the two maps.*

1002

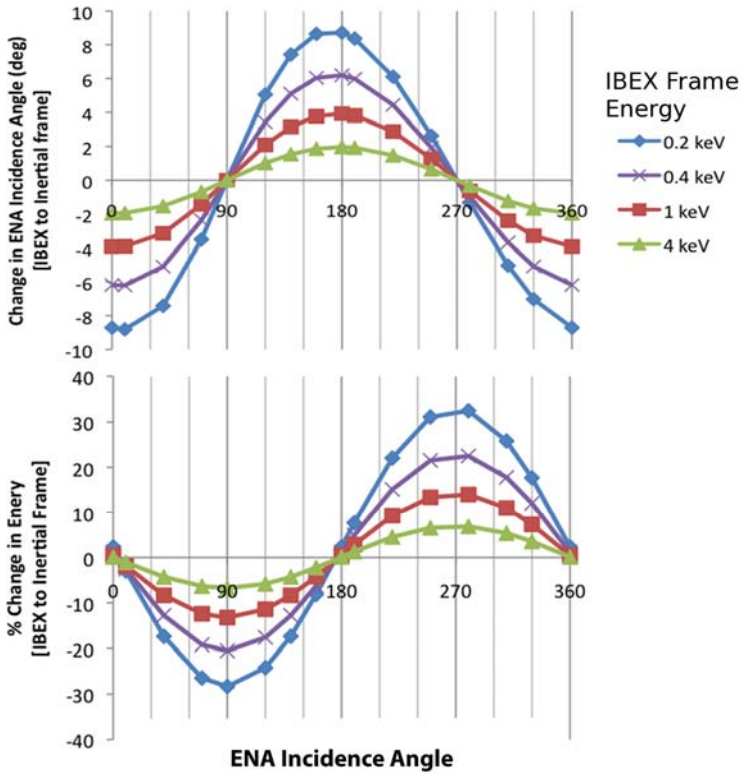


1003

1004 *Figure 10. Energy step 3 (1.1 keV) sky map showing the three regions used for Table 2:*

1005 *1) the ribbon, 2) the nose and N pole region, and 3) the tail, flanks, and south pole region.*

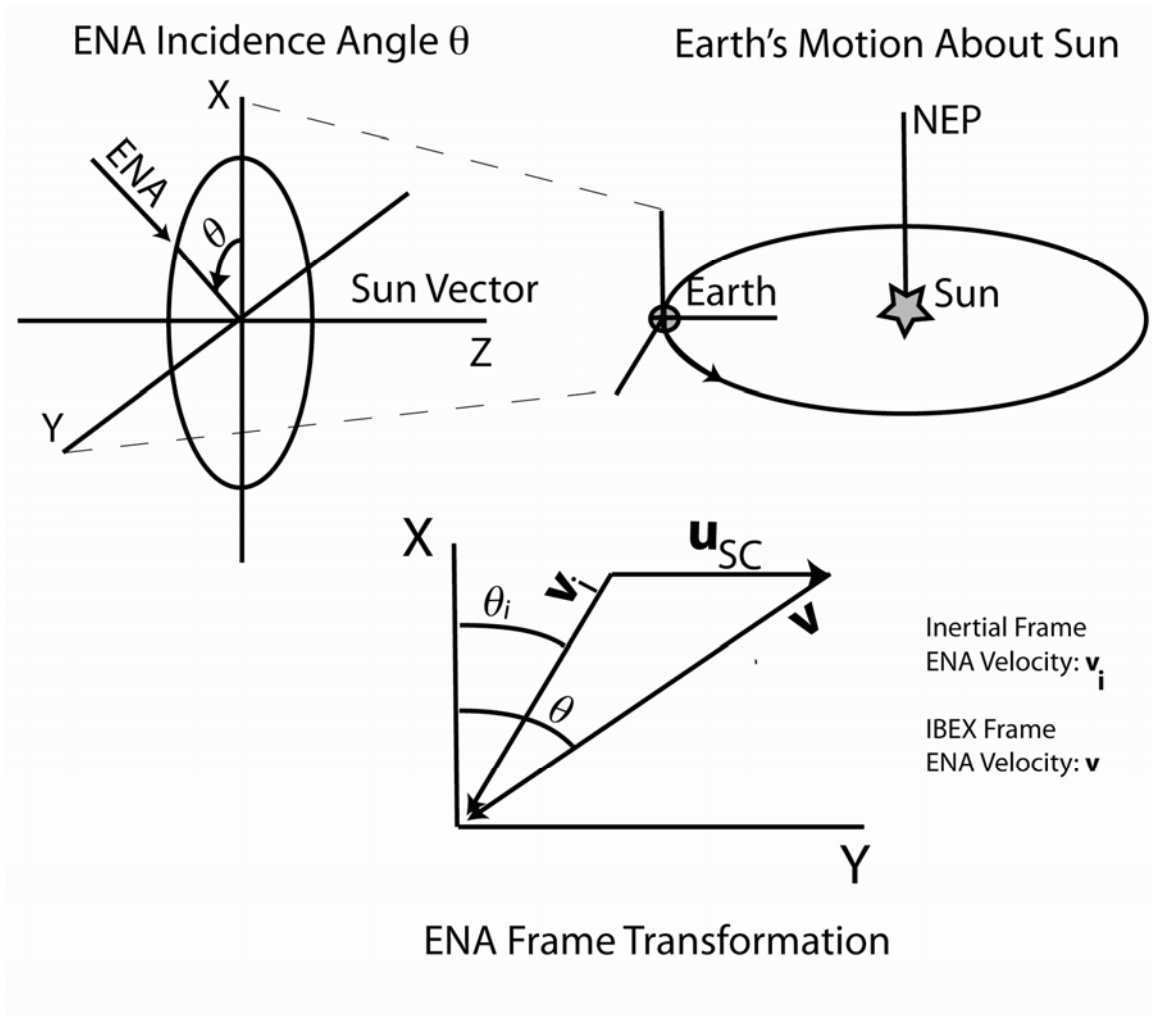
1006



1007

1008 *Figure A1. The change in ENA incidence angle (top) and energy (bottom) from the IBEX*
 1009 *reference frame to the inertial frame as a function of the ENA incidence angle measured*
 1010 *from the North-Ecliptic Pole (NEP) in the spacecraft frame. The spacecraft rotates about*
 1011 *the spin axis directed approximately toward the Sun, with each of the sensors directed*
 1012 *approximately perpendicular to the spin axis. A sensor measures an ENA incidence angle*
 1013 *of 0° where the sensor bore sight points to the NEP (See Figure A2). Since the spacecraft*
 1014 *spins in a right-handed sense, an ENA incidence angle of 90° is measured where the*
 1015 *sensor bore sight is directed roughly along the vector of Earth's motion about the Sun.*
 1016 *An ENA incidence angle of 180° is measured where the bore sight is directed along the*
 1017 *South-Ecliptic Pole, and an incidence angle of 270° is measured where the bore sight is*
 1018 *directed opposite to Earth's motion.*

1019



1020

1021 *Figure A2. The motion of Earth about the Sun makes it necessary to transform ENA*
 1022 *measurements from the IBEX reference frame to an inertial reference fixed with the Sun.*
 1023 *The geometry of this frame transformation is illustrated here. The IBEX spacecraft has*
 1024 *an approximately Sun-pointed spin axis, and we measure incident ENAs in the spin-plane*
 1025 *roughly perpendicular to the spin-axis. (Top-left) The incident ENA velocity angle, θ , is*
 1026 *measured relative to the NEP (X-axis) in the spin-plane as a right-handed rotation about*
 1027 *the Z-axis. (Top-right) The Y-axis is directed along the vector of Earth's motion around*
 1028 *the Sun. (Bottom) In the spin-plane, the inertial frame ENA velocity, \mathbf{v}_i , is the sum of the*
 1029 *spacecraft velocity, \mathbf{u}_{SC} , and the measured ENA velocity, \mathbf{v} .*

1030 Table 1. Energy passbands for IBEX-Hi (qualified triple-coincidence detections)

E-Step	E _{-FW}	E _{-FWHM}	E _{Nominal}	E _{+FWHM}	E _{+FW}	$\Delta E/E$
	[keV]	[keV]	[keV]	[keV]	[keV]	FWHM
2	0.35	0.52	0.71	0.95	1.23	0.60
3	0.58	0.84	1.08	1.55	1.93	0.65
4	1.07	1.36	1.85	2.50	3.02	0.62
5	1.68	1.99	2.70	3.75	4.54	0.65
6	2.57	3.13	4.09	6.00	6.93	0.70

1031

1032 Table 2. Ratios of ENA fluxes in second maps compared to first maps.

Energy (keV)	Ratio of weighted fluxes ($F_{\text{Map-2}}/F_{\text{Map-1}}$)			
	1) Ribbon	2) Nose/N pole	3) Tail/Flanks/S pole	All Sky
~0.7	0.89 ± 0.03	0.95 ± 0.03	0.67 ± 0.01	0.79 ± 0.01
~1.1	0.90 ± 0.02	0.99 ± 0.02	0.79 ± 0.01	0.87 ± 0.01
~1.7	0.98 ± 0.02	1.02 ± 0.02	0.92 ± 0.01	0.98 ± 0.01
~2.7	0.96 ± 0.01	0.98 ± 0.01	0.96 ± 0.01	0.97 ± 0.01
~4.3	0.91 ± 0.01	0.92 ± 0.01	0.92 ± 0.01	0.92 ± 0.01

1033

1034 Table 3. 100 AU transit times for ENAs in IBEX-Hi energy passbands.

E-Step	E _{-FW}	E _{-FWHM}	E _{Nominal}	E _{+FWHM}	E _{+FW}
	[days]	[days]	[days]	[days]	[days]
2	668	580	469	405	356
3	519	431	380	317	284
4	382	339	290	250	227
5	305	280	240	204	185
6	247	223	195	161	150

1035